Phase transition analogs in laser collisions with a dark-field setup

Holger Gies,[*] Felix Karbstein,[†] and Lars Maiwald[‡]

Theoretisch-Physikalisches Institut, Abbe Center of Photonics, Friedrich-Schiller-Universität Jena, Max-Wien-Platz 1, 07743 Jena, Germany;
Helmholtz-Institut Jena, Fröbelstieg 3, 07743 Jena, Germany;
and GSI Helmholtzzentrum für Schwerionenforschung, Planckstraße 1, 64291 Darmstadt, Germany

(Received 27 November 2024; accepted 11 January 2025; published 30 January 2025)

Laser pulse collisions are a promising tool for the investigation of light-by-light scattering phenomena induced by quantum vacuum fluctuations. Using the numerical code based on the vacuum emission picture and put forward in [1], we observe a strong dependence of the signal features on the transverse profiles of the colliding laser pulses in the interaction region. For a probe beam tailored such as to feature an annular far-field profile and a pronounced on-axis focus peak counterpropagating a pump beam at zero impact parameter, the signal's main emission direction can undergo the analog of a phase transition with the beam-waist ratio of the pulses serving as a control parameter. Depending on the pump's beam profile, this phase transition can be first order (e.g., for a pump with a flat-top far-field profile) or second order (e.g., for a Gaussian pump). From the simulation data, we determine the critical point and extract the corresponding critical exponent for the second-order transition of the main emission direction of the signal in the far field. For this, we improve the performance of the above numerical code, using the phase transition analogs as an example to illustrate the capabilities and limitations of the code and current workflows.

DOI: 10.1103/PhysRevD.111.016027

I. INTRODUCTION

Nonlinear interactions of electromagnetic fields in vacuum are a long-standing prediction of quantum electrodynamics (QED) [2,3]. For a precise and quantitative verification of these interactions, the collision of macroscopically controllable, ultra-intense laser pulses is a promising experimental pathway in many laboratories worldwide. This could provide access to the plethora of phenomena induced by quantum vacuum fluctuations of charged matter degrees of freedom; see [4–10] for reviews.

The direct route to experimental investigation is hampered by the diminutiveness of the effect, as can be seen on the quantum level from the small photon-photon cross section at low frequency [11–14], requiring a careful and delicate separation of the small signal from the expectably large background. Many ideas and concepts have been put forward in recent years to solve this problem; cf., e.g., [15–26]. A particularly promising idea is the use of tailored probe beams in order to realize a dark-field setup, which combines the virtues of a geometrical signal-to-background separation with the still sizable scattering rates in the forward direction of the probe in a comparatively simple configuration involving only two counterpropagating beams [21,23,27]. A similar scheme has already experimentally proved of value in high-harmonic generation [28,29] and has become a cornerstone of an intended discovery experiment of vacuum birefringence at the HED-HIBEF beamline at the European XFEL [30].

While theoretical tools for the prediction of observables for realistic laser pulses have also evolved substantially in the past years (see [10,31] and references therein), analytical methods are often limited to validity regimes of necessary approximations. A particularly efficient analytical modeling of realistic laser pulses is often achieved by using paraxial beams together with the approximation of taking the formal limit of an infinite Rayleigh range [32,33]. This approximation can, for instance, be quantitatively well controlled for nonextremal focusing and sufficiently small pulse durations [34].

For general beams and collision geometries, powerful numerical methods are highly desired. In addition to methods that aim at numerically solving the QED-induced nonlinear Heisenberg-Euler-Maxwell equations in a general fashion [35–37], methods that are designed to directly compute the relevant observables have turned out to be particularly fruitful for the description of pulse collisions. In the present work, we use the VacEm code [1] which is based on the vacuum emission picture [38,39]. The latter

[*]Contact author: holger.gies@uni-jena.de
[†]Contact author: felix.karbstein@uni-jena.de
[‡]Contact author: lars.maiwald@uni-jena.de

effectively reduces the computation of the quantum-induced signatures to performing a space-time Fourier transformation of the field distribution in the interaction region; the corresponding numerical task can be faced in various ways [18,40,41]. Specifically, the VacEm code has been used in various studies requiring quantitative accuracy [1,27,42,43].

In the present work, we highlight and analyze a phenomenon in the quantum-vacuum signatures of colliding pulses that is reminiscent of a phase transition in statistical physics. We demonstrate that both its qualitative and quantitative properties depend sensitively on the beam properties such that the use of an accurate computational method is mandatory. More specifically, we use a *probe* beam with an annular far-field profile but a pronounced on-axis peak in the focus colliding head on with a strong *pump* pulse, and we study the angular distribution of quantum-induced signal photons arising from the interaction region. We confirm that the far-field emission characteristics of the signal can be peaked either in the direction of the probe's beam axis or at a finite angular offset [21] depending on various details, specifically the relative beam waists of the colliding pulses and the transverse beam profiles.

Interestingly, our results can be phrased in the language of critical phenomena with the main emission direction of the signal serving as an order parameter that can undergo an apparent symmetry transition from on axis to off axis depending on the pump properties serving as control parameters. As the computation of observables in the critical region—specifically the location of the phase transition, its order, and a corresponding critical exponent in the case of a second-order transition—requires a substantial numerical accuracy, we use the present investigation also as a motive to improve the VacEm code as well as study its convergence with critical discretization parameters, as initiated in [44]. We observe that the accurate modeling of flat-top beam profiles, which are rather generic in experiments, can pose a numerical challenge. Addressing this challenge, our code improvements target the computational cost. More specifically, the improvements significantly reduce the computation time, memory, and storage demand. The extensive simulations of flat-top beams are thus made feasible in practice.

Our suggestion to phrase the quantum vacuum phenomena studied in this work in terms of critical phenomena may be useful for future studies of possible aspects of universality of the transition phenomenon. Specifically, second-order phase transitions in statistical systems exhibit a large degree of universality induced by fluctuations and near-conformal self-similar behavior in the vicinity of the phase transition [45–47]. The language of critical phenomena has also been useful in the characterization of gravitational collapse [48,49] as well as QED vacuum decay in terms of the Schwinger effect [50,51] with the degree of universality being an active research field in each of these cases [52–57]. Within strong-field QED, a critical point has also been discovered in the momentum spectrum for nonlinear Breit-Wheeler pair production with the width of the photon wave packet serving as a control parameter [58].

This article is organized as follows: Section II provides a brief introduction to the vacuum emission picture, explains how numerical simulations allow us to study arbitrary field configurations, and discusses the capabilities and limitations of our current approach. Section III elucidates the use of tailoring laser fields to achieve certain desired signal profiles. Here, we demonstrate that our results for laser pulse collisions can be phrased in terms of a phase transition analog. At the same time, our work serves as an illustration of the broad abilities of the improved VacEm code. Section IV concludes this work and presents an outlook. Appendixes A–C provide the technical details for code improvements, artifact suppression, and error estimation.

In line with the literature, we use Heaviside-Lorentz units with $c = \hbar = \varepsilon_0 = 1$ and the metric $g^{\mu\nu} = \mathrm{diag}(-1,+1,+1,+1)$ for the conceptual discussion; the numerical code as well as the description in the corresponding sections below use SI units and the metric $g^{\mu\nu} = \mathrm{diag}(1,-1,-1,-1)$.

II. SIGNAL PHOTONS IN THE VACUUM EMISSION PICTURE

Let us briefly summarize the formalism for computing the signatures of quantum vacuum nonlinearities in high-intensity laser pulse collisions. We pay special attention to the assumptions, approximations, and the resulting analytical error. We focus on the numerical simulation of these signatures, discussing the parameters which control simulation accuracy and cost.

A. Vacuum emission picture

We start from the one-loop Heisenberg-Euler Lagrangian to leading order in a weak-field expansion [11],

$$\mathcal{L}_{\mathrm{HE}}^{\text{1-loop}} = \frac{\alpha}{90\pi}\frac{4\mathcal{F}^2+7\mathcal{G}^2}{E_{\mathrm{cr}}^2} + O(F^6), \tag{1}$$

with elementary charge e, electron mass m_e, and also setting the scale for the critical field strength, $E_{\mathrm{cr}} = \frac{m_e^2}{e} \approx 1.32 \times 10^{18}$ V/m. The weak-field expansion is formulated in terms of the relativistic invariants

$$\mathcal{F} = \frac{1}{4}F_{\mu\nu}F^{\mu\nu} = \frac{1}{2}(\boldsymbol{B}^2 - \boldsymbol{E}^2), \tag{2a}$$

$$\mathcal{G} = \frac{1}{4}F_{\mu\nu}\tilde{F}^{\mu\nu} = -\boldsymbol{B}\cdot\boldsymbol{E}. \tag{2b}$$

Here, $F^{\mu\nu}$ denotes the field strength tensor of the applied electromagnetic field and $\tilde{F}^{\mu\nu} = \frac{1}{2}\varepsilon^{\mu\nu\alpha\beta}F_{\alpha\beta}$ its Hodge dual.

The higher orders in Eq. (1) are suppressed by corresponding powers of the critical field strength and can be derived to arbitrarily high order from the full expression, cf. [2,4,9,59].

Equation (1) is the relevant interaction term for the study of signatures of quantum vacuum nonlinearities in currently achievable high-intensity laser pulse collisions. In addition to the weak-field expansion and the one-loop approximation, it relies on the assumption of the fields varying slowly on scales of the (reduced) Compton wavelength $\lambda\!\!\!^{-}_{\mathrm{C}} \approx 3.86 \times 10^{-13}$ m and Compton time $\tau_{\mathrm{C}} \approx 1.29 \times 10^{-21}$ s. For state-of-the-art and near-future laboratory parameters, the dominant error arises from the loop expansion with the subleading two-loop terms contributing corrections on the 1% level. While the latter are fully computable [4,60–62], we consider this as an incentive to aim for a numerical error well below this higher-loop level such that numerical predictions can reliably cover two-loop accuracy in future studies.

In the vacuum emission picture, the signal amplitude follows as

$$\mathcal{S}_{(p)}(\boldsymbol{k}) = \langle \gamma_\beta(\boldsymbol{k}) | \Gamma^{\text{1-loop}}_{\text{HE}} | 0 \rangle, \tag{3}$$

where $\langle \gamma_\beta(\boldsymbol{k})|$ is the one photon state with linear polarization $\beta \in [0, 2\pi)$ and wave vector $\boldsymbol{k}$. The interaction of the colliding laser pulses is encoded in the effective action $\Gamma^{\text{1-loop}}_{\text{HE}} = \int \mathrm{d}^4x\, \mathcal{L}^{\text{1-loop}}_{\text{HE}}$, and $|0\rangle$ denotes the vacuum state. We emphasize that Eq. (3) accounts only for the zero-to-one signal-photon transition. Processes generating two or more signal photons are neglected, as they are typically suppressed relative to the single signal-photon emission [63].

To evaluate Eq. (3), we decompose the field as $F^{\mu\nu} \to F^{\mu\nu} + f^{\mu\nu}$ into an intense background $F^{\mu\nu}$ treated as classical and $f^{\mu\nu}$ considered as an operator-valued signal. For the one-signal-photon amplitude, it suffices to consider the leading order of the expansion of Eq. (1) around the background,

$$\mathcal{L}^{\text{1-loop}}_{\text{HE}}(F+f) = \mathcal{L}^{\text{1-loop}}_{\text{HE}}(F) + f^{\mu\nu} \frac{\partial \mathcal{L}^{\text{1-loop}}_{\text{HE}}(F)}{\partial F^{\mu\nu}} + O(f^2). \tag{4}$$

Combining Eqs. (1)–(4), we can write the signal amplitude as [32]

$$\mathcal{S}_\beta(\boldsymbol{k}) = \mathcal{A} \int \mathrm{d}^4x\, \mathrm{e}^{\mathrm{i}kx} \times [4(\boldsymbol{e}_\beta \cdot \boldsymbol{E} - \boldsymbol{e}_{\beta+\frac{\pi}{2}} \cdot \boldsymbol{B})\mathcal{F} + 7(\boldsymbol{e}_\beta \cdot \boldsymbol{B} + \boldsymbol{e}_{\beta+\frac{\pi}{2}} \cdot \boldsymbol{E})\mathcal{G}], \tag{5}$$

where $\mathcal{A} = \frac{1}{\mathrm{i}} \frac{e}{4\pi^2} \frac{m_e^2}{45} \sqrt{\frac{\mathrm{k}}{2}} (\frac{e}{m_e^2})^3$, and $\mathrm{k} = k^0 = |\boldsymbol{k}|$ denotes the wave number. The linear polarization vectors $\boldsymbol{e}_\beta(\boldsymbol{k}), \boldsymbol{e}_{\beta+\frac{\pi}{2}}(\boldsymbol{k})$ form an orthonormal basis together with the normalized wave vector $\boldsymbol{e}_{\boldsymbol{k}} = \boldsymbol{k}/\mathrm{k}$. We also use the short form $kx = k^\mu x_\mu$. The (energy and emission angle resolved) differential number of signal photons is given by

$$\frac{\mathrm{d}^3 N_\beta(\boldsymbol{k})}{\mathrm{d}^3\mathrm{k}} = \frac{1}{(2\pi)^3} |\mathcal{S}_\beta(\boldsymbol{k})|^2, \tag{6}$$

where $\mathrm{d}^3\mathrm{k} = \mathrm{k}^2\, \mathrm{d}\mathrm{k}\, \mathrm{d}\Omega$ and $\mathrm{d}\Omega = \sin(\vartheta)\mathrm{d}\vartheta\, \mathrm{d}\varphi$. In this work, we do not resolve signal-photon polarizations but sum over both orthogonal polarization directions. Of course, the VacEm code provides fully polarization resolved information.

B. Numerical implementation

The VacEm code is a numerical simulation code introduced in [1]. Given an arbitrary EM field configuration and parameters defining the simulation domain, it computes the signal amplitude Eq. (5) in two parts $\mathcal{S}_{\mathrm{a/b}}$ such that $\mathcal{S}_\beta(\boldsymbol{k}) = \mathcal{A}(\sin(\beta)\mathcal{S}_{\mathrm{a}}(\boldsymbol{k}) + \cos(\beta)\mathcal{S}_{\mathrm{b}}(\boldsymbol{k}))$. In order to reduce the number of operations and enable using fast Fourier transform (FFT) for the main computational task, the implementation works with the reformulated equations

$$\mathcal{S}_{\mathrm{a}}(\boldsymbol{k}) = \int \mathrm{d}t\, \mathrm{e}^{\mathrm{i}c\mathrm{k}t} [\boldsymbol{e}_1 \cdot \hat{\boldsymbol{Q}} - \boldsymbol{e}_2 \cdot \hat{\boldsymbol{R}}], \tag{7a}$$

$$\mathcal{S}_{\mathrm{b}}(\boldsymbol{k}) = \int \mathrm{d}t\, \mathrm{e}^{\mathrm{i}c\mathrm{k}t} [\boldsymbol{e}_2 \cdot \hat{\boldsymbol{Q}} + \boldsymbol{e}_1 \cdot \hat{\boldsymbol{R}}], \tag{7b}$$

where $\boldsymbol{e}_1$ and $\boldsymbol{e}_2$ denote some basis vectors for the polarization direction such that $\boldsymbol{e}_\beta(\boldsymbol{k}) = \sin(\beta)\boldsymbol{e}_1(\boldsymbol{k}) + \cos(\beta)\boldsymbol{e}_2(\boldsymbol{k})$. We define

$$\hat{\boldsymbol{Q}} = \int \mathrm{d}^3x\, \mathrm{e}^{-\mathrm{i}\boldsymbol{k}\cdot\boldsymbol{x}} \boldsymbol{Q} \quad \text{with} \quad \boldsymbol{Q} = 4\boldsymbol{E}\mathcal{F} + 7\boldsymbol{B}\mathcal{G}, \tag{8a}$$

$$\hat{\boldsymbol{R}} = \int \mathrm{d}^3x\, \mathrm{e}^{-\mathrm{i}\boldsymbol{k}\cdot\boldsymbol{x}} \boldsymbol{R} \quad \text{with} \quad \boldsymbol{R} = -4\boldsymbol{B}\mathcal{F} + 7\boldsymbol{E}\mathcal{G}. \tag{8b}$$

The numerical implementation is now straightforwardly given by $\int \mathrm{d}t \to \sum_t \Delta t$ and $\int \mathrm{d}^3x\, \mathrm{e}^{-\mathrm{i}\boldsymbol{k}\cdot\boldsymbol{x}} \to \mathrm{FFT}_3$; see Appendix A for a pseudocode representation.

The simulation grid (in position space) is controlled by 8 parameters. There are 4 parameters defining the simulation domain (L_t, L_x, L_y, L_z) and 4 parameters defining the number of grid points in each dimension (N_t, N_x, N_y, N_z). There are multiple aspects to consider when choosing these parameters. The simulation grid must capture the interaction of the laser pulses in extent and resolution. Furthermore, the numerical error generally shrinks for larger parameter values, but the computational cost grows. The former is a minimum requirement, whereas the latter is an optimization problem.

It is useful to consider the grid resolution $(\Delta t, \Delta x, \Delta y, \Delta z)$ with $\Delta\mu = L_\mu/N_\mu$. Focusing on the counterpropagating scenario, the relevant scales for the temporal parameters are set by the pulse durations τ_i and wavelengths λ_i, where $i \in \mathbb{N}$ labels the laser pulse, i.e., $L_t = L_t(\tau_i)$, $\Delta t = \Delta t(\lambda_i)$. We require a sufficiently small Δt in order to achieve convergence of the time integration. For the spatial parameters, we connect the longitudinal extent along the beam axis to the extent in time $L_\parallel = L_\parallel(L_t)$ and adjust the transversal extent $L_\perp = L_\perp(w_{0,i})$ as a function of the beam waists $w_{0,i}$.

Similar considerations can be made in $\boldsymbol{k}$ space. Since $\Delta k_{x,y,z} = 2\pi/L_{x,y,z}$ and $k_{x,y,z,\max} \approx 2\pi/(2\Delta x_{x,y,z})$, the desired/required $\boldsymbol{k}$ space properties constrain the choice of the spatial parameters $L_{x,y,z}$ and $N_{x,y,z}$.

Computational cost is only affected by N_μ. The required number of operations scales with $N_t N_x N_y N_z \log(N_x N_y N_z)$ and the required memory with $N_x N_y N_z$. We are mainly limited by memory, in particular, memory size. Appendix A provides insight into the memory usage. Memory bandwidth and latency additionally play a crucial role when considering the processor-memory bottleneck (performance gap) [64]. The original VacEm code runs on one node and calls `FFTW` [65,66] for parallel FFT_3. In this work, improvements to the computation time and memory usage were implemented. Multinode parallelism of the time integration and single-precision float operations were added to the feature set; see Appendix A and [44]. To resolve the still existent memory bottleneck, FFT_3 with distributed-memory parallelism should be implemented in the future.

Given the current code status and hardware performance, a careful choice of all 8 simulation domain parameters can largely suppress numerical artifacts at a reasonable computational cost. Aliasing can be avoided by choosing $\Delta\mu$ such that the sampling rate is above the Nyquist rate of the involved frequencies. Spectral leakage caused by windowing is unavoidable and can only be suppressed by increasing $L_{x,y,z}$. In Sec. III, we quantify the impact of numerical artifacts. This work demonstrates the current capabilities of the VacEm code.

III. QUANTUM-VACUUM SIGNATURES FROM TAILORED-PULSE COLLISIONS

A. Pulse collisions in a dark-field scheme

Collisions of ultra-intense laser pulses lead to the generation of scattered photons as a signature of the fluctuation-induced effective nonlinear interactions between electromagnetic fields and thus of the violation of the superposition principle by the quantum vacuum. With two generic laser pulses, the largest signal is produced in a counterpropagating head-on collision. However, a straightforward detection in experiment is hampered by the fact that the quantum-induced signal photons are predominantly scattered into the forward direction [8,9]. This makes it challenging to separate the signal from the huge photon background of the driving laser pulses.

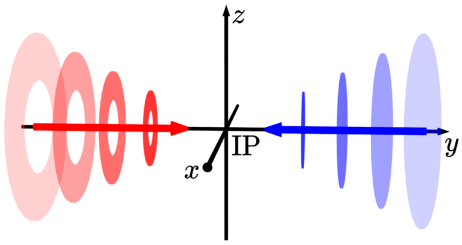

FIG. 1. Sketch of the collision setup showing the annular flat-top probe in red propagating towards the positive y direction and the counterpropagating Gaussian or flat-top pump in blue colliding in the interaction point (IP) at $(x, y, z) = (0, 0, 0)$. The increasing opacity indicates the evolution forward in time. The colored arrows indicate their respective propagation directions.

A promising idea to address this challenge is given by the dark-field scheme [21,23] which we also use in the following. Here, an annular pulse is tailored by blocking a central part of the transverse far-field profile of the incoming pulse such that the outgoing pulse also features a field-free central region around its beam axis while a peaked on-axis field is retained in its focus. This tailored pulse is considered as the probe pulse going into the positive y direction in our setup; see Fig. 1. The probe pulse hits a counterpropagating pump pulse, both considered to be optimally aligned at the collision point, which we choose as the origin of our coordinate system. A crucial point now is that the signal photons being scattered into the forward direction of the probe pulse have the chance to propagate into the forward shadow of the annular pulse. If the shadow is sufficiently dark, a detector positioned inside the dark-field region has the chance to detect the signal photons above the shadow-suppressed background.

Focusing on the signal in the forward direction of the probe, the dominant contribution to the signal amplitude stems from the interaction in the focus region. Due to energy and momentum conservation, the dominant term in the signal amplitude Eq. (5) is linear in the probe and quadratic in the pump pulse, cf. [63],

$$\mathcal{S}_\beta(\boldsymbol{k})|_{\sim E_{\mathrm{probe}}} \propto \int \mathrm{d}^4x\, \mathrm{e}^{\mathrm{i}kx}[E_{\mathrm{probe}}(x)|E_{\mathrm{pump}}(x)|^2 \times \Theta(\theta, \varphi, \beta)], \tag{9}$$

where Θ is some function defining the details of the angular dependence. Therefore, it is instructive to take a closer look at the probe field and the pump intensity in the focus.

More specifically, we use a pulsed annular flat-top beam as the probe field, while we study both a pulsed Gaussian beam or a pulsed flat-top beam as the pump field. In the focal (x, z) plane, we choose the polarization of both beams in the z direction.

The annular flat top and its special case, the flat top, are analytically known in the interaction region. A Maxwell solver makes them available at any time step t; see Appendix A. For instance, the electric field component of a linearly polarized beam (oscillation frequency ω_{I}) propagating in the y direction ($\rho = \sqrt{x^2 + z^2}$) in the focus region is given by [63]

$$E_{\mathrm{I}}(t,\boldsymbol{x}) = 2E_0\sqrt{\frac{1-1/\mathrm{e}}{1+\nu}}\mathrm{e}^{-\left(\frac{y-t}{\tau_{\mathrm{I}}/2}\right)^2} \times\left[\frac{J_1\left(\sqrt{\frac{2(1-1/\mathrm{e})}{1+\nu}}\frac{2\rho}{w_{\mathrm{I}}}\right)}{\sqrt{\frac{2(1-1/\mathrm{e})}{1+\nu}}\frac{2\rho}{w_{\mathrm{I}}}} - \nu\frac{J_1\left(\sqrt{\frac{2(1-1/\mathrm{e})}{1+\nu}}\nu\frac{2\rho}{w_{\mathrm{I}}}\right)}{\sqrt{\frac{2(1-1/\mathrm{e})}{1+\nu}}\nu\frac{2\rho}{w_{\mathrm{I}}}}\right] \times\cos(\omega_{\mathrm{I}}(y-t)), \tag{10}$$

with the corresponding Gaussian peak field amplitude [67]

$$E_0 = \sqrt{8\sqrt{\frac{2}{\pi}}\frac{W_{\mathrm{I}}}{\pi w_{\mathrm{I}}^2\tau_{\mathrm{I}}}} \tag{11}$$

expressed in terms of the pulse energy W_{I}, waist w_{I}, and $1/\mathrm{e}^2$ (on intensity level) pulse duration τ_{I}. The subscript I emphasizes the validity limited to the interaction region, J_1 is the Bessel function of first kind at order 1, and $\nu = (\theta_{\mathrm{in}}/\theta_{\mathrm{out}})^2$ is the blocking fraction for the annular flat top with inner and outer far-field radial divergences θ_{in}, θ_{out}. In the remainder of this work, we assume $\nu = 1/4$ for the annular flat top and, of course, $\nu = 0$ for the flat top.

In Fig. 2, we depict the transverse focus profiles of the annular flat-top beam amplitude, and of the intensities for the flat-top beam and the Gaussian beam along the transversal x direction; cf. Eq. (9). Throughout this work, the pulse parameters are given by the wavelength $\lambda = 800$ nm, pulse duration $\tau_{\mathrm{FWHM}} = 20$ fs$(=\sqrt{\ln(2)/2}\tau)$, and pulse energy $W = 25$ J corresponding to a petawatt-class high-intensity pulse. We somewhat arbitrarily keep the probe's beam waist fixed at $w_{0,1} \approx 2.18$ μm. The pump's beam waist $w_{0,2}$ is varied to obtain different ratios $w_{0,2}/w_{0,1}$. While the relative polarization could be optimized for certain observables such as polarization flip or total photon yield [67], it is not really of importance for our purpose since it just modifies the overall factor for the signal amplitude.

From Fig. 2, it is obvious that the Gaussian beam has a Gaussian transversal profile in the focal plane. By contrast, the flat-top beams exhibit a nontrivial Airy-ring structure in the focal plane. Because the quantum vacuum signal is peak-field driven, it is clear that the dominant contribution to the signal will arise from the focal region where the maxima of both pulses have the largest overlap. On the other hand, it is also clear that the precise angular distribution of the signal photons depends on the details of the laser beam structure.

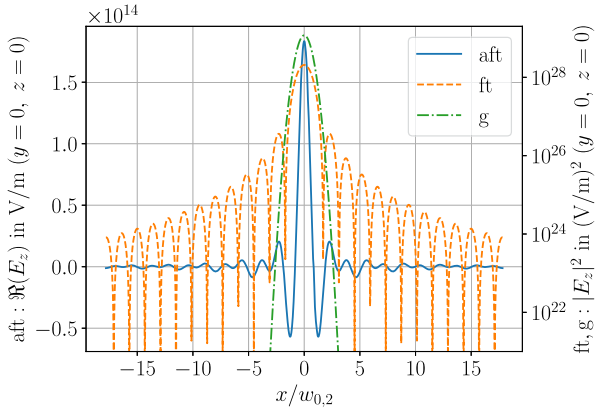

FIG. 2. Transverse profile of the probe amplitude (aft) and the pump intensity (ft, g) in the focus; cf. Eq. (9) (aft: annular flat top; ft: flat top; g: Gaussian; $w_{0,2}/w_{0,1} = 1.9$; see text for all other relevant parameters).

In particular, the much richer transverse structure of a flat-top pump suggests a qualitative difference of the behavior of the angular signal distribution in comparison to that driven by a Gaussian pump.

B. A phase transition analog

In the present work, we focus on a specific phenomenon of the angular signal-photon distribution which can be phrased in the language of a phase transition. As symmetries play a prominent role in the theory of phase transitions, we first note that in the present counterpropagating setup the composite field profile of the colliding laser pulses features a rotational O(2) symmetry about the propagation axis. This rotational symmetry is broken on the level of the field vectors. It turns out that this breaking, of course, results in a similar breaking of the rotational symmetry of the quantum-induced signal photons in terms of their transversal polarization state. In addition, the number of signal photons depends on the relative polarization of the colliding pulses [67]. Nevertheless, the polarization-averaged signal-photon amplitude again inherits the rotationally O(2) symmetry.

The following argument illustrates that such a phase transition analog with respect to the realization of this symmetry must exist. In view of Fig. 2, we can envision the possible interaction scenarios depending on the ratio of pump beam waist $w_{0,2}$ and the probe beam waist $w_{0,1}$. Regardless of the pump type, there exist two limiting cases [21]: In the limit of a small pump beam waist $w_{0,2}/w_{0,1} \ll 1$, the pump predominantly interacts with the main peak of the annular flat top, which effectively corresponds to the collision of two pulses with a single-peak focus structure, similar to two Gaussian peaks. Hence, we expect the signal to also exhibit a single peak structure which—due to the O(2) symmetry—should lie on axis in the forward direction (positive y axis).

In the opposite limit of a large pump beam waist $w_{0,2}/w_{0,1} \gg 1$, the pump pulse can be well approximated by a plane wave over the extent of the probe focus region. This implies that the pump cannot transfer a relevant amount of transverse momentum to the probe field. We thus expect the angular distribution of the signal to resemble the probe in the far field. For the present case of an annular probe pulse, we also expect the signal to feature an annular structure in the transverse (x, z) plane.

For instance, for the signal intensity along the x axis at $z = 0$ and in the far field at sufficiently large y, we expect a single-peak structure for $w_{0,2}/w_{0,1} \ll 1$ with the peak at $x = 0$ on axis and a double-peak structure for $w_{0,2}/w_{0,1} \gg 1$ with the peaks at $|x| > 0$ off axis. (Below, we use an angle variable instead of the x axis, but the features remain the same.) Flipping the sign of the signal-photon distribution in the far field, its shape and behavior resemble that of a Landau-Ginzburg-type potential for an order parameter across a phase transition.

For intermediate values of $w_{0,2}/w_{0,1}$, it is clear now that a transition between a single- and a double-peak structure needs to take place. From the analog to a phase transition, we can infer that this transition can occur in various ways: The transition can be smooth, similar to a second-order transition such that the positions of the double peaks evolve continuously from the single peak for increasing $w_{0,2}/w_{0,1}$ as found analytically for the collision of an annular flattened-Gaussian probe with a Gaussian pump beam in [21]. Alternatively, the double peaks can appear in addition to the single peak exhibiting a coexistence of all peaks for a certain interval of $w_{0,2}/w_{0,1}$ values. This would correspond to a first-order phase transition.

C. Numerical simulation

Using the VacEm code with improved performance, we show in the following that both types of transitions can occur depending on the properties of the pump (flat-top vs. Gaussian pump). This difference can again be motivated from Fig. 2. For the case of a Gaussian pump, continuously more and more side peaks (Airy rings) in the focal region of the annular flat top contribute to the interaction the larger the ratio $w_{0,2}/w_{0,1}$. By contrast, for the flat-top pump, the side peaks on the fringes of the focal region go through cycles of alignment and misalignment when varying $w_{0,2}/w_{0,1}$.

Our investigation of the two setups of counterpropagating axisymmetric pulse collisions defined above uses the following simulation parameters: $L_t = 4\tau, L_y \approx 6c\tau, L_{x,z} \approx 18.5 w_{0,2,\max}$ and a grid resolution $\Delta\mu$ equivalent to 7.5 points per period λ/c and wavelength $\tilde{k}_{x,y,z}/(2\pi)$, where $\tilde{k}_{x,y,z}$ are the estimated maximum wave numbers along each spatial axis. At this resolution, we resolve frequencies up to $(\lambda/3)^{-1}$ along the propagation direction. This would even be sufficient to account for photon merging [24,68–73], a nonlinear phenomenon that is found to be strongly suppressed in our setup.

The reasoning behind the choice of $L_{x,y,z}$ is discussed in Appendix B. The simulations make use of single-precision floating-point operations. The latter provide a significant increase in efficiency at basically no impact on the final accuracy of our result, as the numerical error is dominated by other sources; see Appendix A. The pump's beam waist $w_{0,2}$ is varied between 2.0 μm and 8.0 μm in steps of 0.67 μm, i.e., $w_{0,2}/w_{0,1}$ between 0.92 and 3.7 in steps of 0.31. This gives us 10 values for $w_{0,2}$ and encompasses the expected transition region. After establishing this broad range, we zoom in to better resolve the transition. An additional 10 data points are obtained for $w_{0,2}$ between 4.1 μm and 4.6 μm in steps of 0.061 μm, i.e., $w_{0,2}/w_{0,1}$ between 1.9 and 2.1 in steps of 0.028 in order to study the nature of the transition.

We employ the VacEm code to simulate the signal amplitude Eq. (5) for each value of $w_{0,2}$. From this, we compute the corresponding differential number of signal photons, Eq. (6). Our observable of choice for visualizing the resulting data is $\mathrm{d}N/\mathrm{d}\Omega|_{\vartheta=90°}$; i.e., we integrate the differential number of signal photons over k and study it in the (x, y) plane at polar angle $\vartheta = 90°$. The spherical coordinate system (r, ϑ, φ) is defined such that r is the radial distance, ϑ is the polar angle between the z axis and the radial axis, and φ is the azimuthal angle between the x axis and the radial axis. Figures 3 and 4 show the signal profiles for the range of pump beam waists $w_{0,2}$ in the vicinity of the phase transition as a function of the azimuthal angle φ near and across the forward propagation direction $\varphi = 90°$.

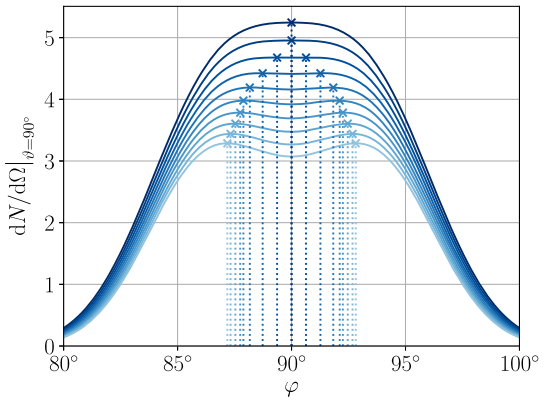

FIG. 3. Differential number of signal photons in the (x, y) plane as a function of the azimuthal angle with $\varphi = 90°$ denoting the forward propagation direction of the probe (annular flat top) and signal. For the Gaussian pump setup, we observe the continuous emergence of a double-peak structure with the pump waist $w_{0,2}$ between 4.1 μm (dark blue) and 4.6 μm (light blue) in steps of 0.061 μm. The peaks of the individual curves are marked by a cross (×). This transition is analogous to a second-order phase transition.

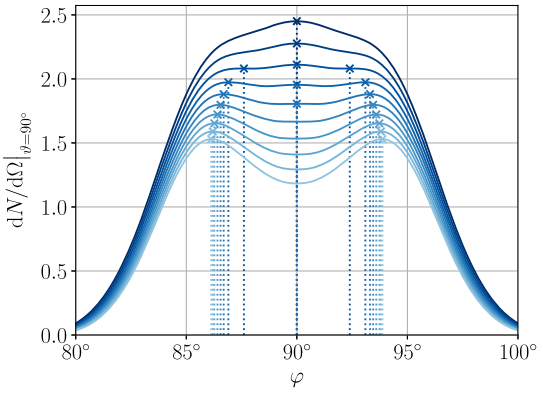

FIG. 4. Differential number of signal photons in the (x, y) plane as a function of the azimuthal angle with $\varphi = 90°$ denoting the forward propagation direction of the probe (annular flat top) and signal. For the flat-top pump setup, the double-peak structure emerges while the central peak still exists. The graphs span a range of pump waists $w_{0,2}$ between 4.1 μm (dark blue) and 4.6 μm (light blue) in steps of 0.061 μm. The peaks of the individual curves are marked by a cross (×). This transition is analogous to a first-order phase transition.

In Fig. 3, we depict the data for the collision of the annular flat-top probe with the Gaussian pump for pump waists $w_{0,2}$ between 4.1 μm (dark blue) and 4.6 μm (light blue) in steps of 0.061 μm. The topmost dark blue curve in Fig. 3 belongs to the smallest pump waist $w_{0,2}$, exhibits a single-peak structure on the propagation axis at $\varphi = 90°$, and resembles a flattened Gaussian [74]. For even smaller $w_{0,2}$ (not shown in the figure), the signal profile converges towards a Gaussian shape. For increasing pump waist $w_{0,2}$, the central peak broadens even further and evolves smoothly into a double peak with the two peaks moving further outward away from the propagation axis [21]. The main emission directions are marked by a cross (×). The transition from the single peak on axis to the double peaks off axis is continuous and—using the peak position φ_{peak} (in the branch $\varphi \geq 90°$) as an order parameter—resembles a phase transition of second order.

In Fig. 4, we show the data for the collision of the same probe (annular flat top) with the flat-top pump for the same range of pump beam waists. The particular features of the topmost dark blue curve can be explained by the already growing left and right peaks. For smaller $w_{0,2}$ (not shown in the figure), this effect is not yet visible, and a Gaussian shape is approached. For an increasing pump beam waist $w_{0,2}$, the side peaks become more pronounced, and we observe a coexistence region of $w_{0,2}$ values where the side peaks as well as the central peak are local maxima marked by a cross (×). This coexistence makes the transition resemble a first-order phase transition. For larger $w_{0,2}$ beyond the coexistence region, the differential number of signal photons on the propagation axis at $\varphi = 90°$ becomes a local minimum. The lowermost light blue curve belongs to the largest $w_{0,2}$ values of the plot.

From the markings, a qualitative difference in the transition process, as compared to the analogous scenario with a fundamental Gaussian pump, is evident. Counterpropagating axisymmetric collision of the annular flat-top probe and the Gaussian pump in Fig. 3 shows a continuous formation of the left and right peaks from the center. The central peak effectively dissolves into the outer peaks. In contrast, the counterpropagating axisymmetric collision of the annular flat-top probe and the flat-top pump in Fig. 4 shows that the outer peaks start to form independently of the central peak. There is even a period during the transition where the outer peaks and the central peak exist simultaneously.

Both figures clearly reflect the expectations of the limiting cases: For a small pump beam waist, only the interactions of the central focal peaks are relevant and lead to a formation of a signal peak on axis. For larger pump beam waists, the pump eventually resembles a plane wave and the signal takes over the annular far-field profile of the probe. Of course, for the beam waists shown in the figures, we are still far away from the plane-wave limit $w_{0,2}/w_{0,1} \to \infty$.

To further quantify the transition, we study the dependence of the main emission direction of the signal photons φ_{peak} (in the branch $\varphi \geq 90°$) on the beam-waist ratio $w_{0,2}/w_{0,1}$ in Figs. 5 and 6.

In these plots, we include a broader range of $w_{0,2}$ values than used in Figs. 3 and 4. In the language of critical phenomena, it is obvious from these figures that the beam-waist ratio $w_{0,2}/w_{0,1}$ can be identified as a control

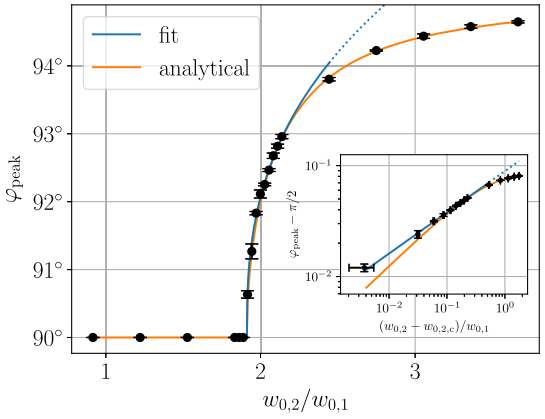

FIG. 5. Main emission direction of the far-field signal-photon distribution for an annular flat-top probe colliding with a Gaussian pump as a function of the pump-to-probe waist ratio $w_{0,2}/w_{0,1}$ across the transition. Interpreting the main emission direction (in the branch $\varphi \geq 90°$) as an order parameter, we observe a continuous second-order phase transition. The blue curve represents the power-law fit Eq. (12) for the critical parameters of the transition region. The orange curve depicts the analytical estimate (13). The double logarithmic plot in the inset illustrates that the critical region is well described by this simple scaling law Eq. (12) with a critical exponent $\boldsymbol{\beta}$.

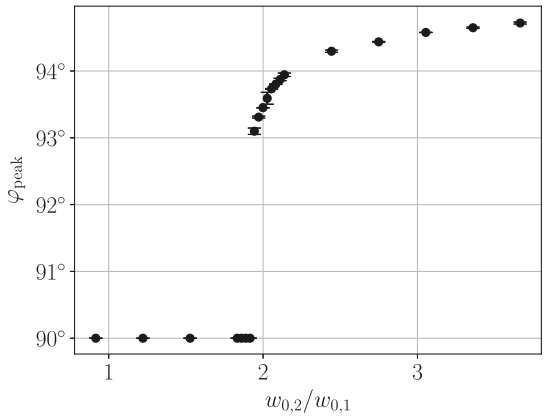

FIG. 6. Main emission direction of the far-field signal-photon distribution for an annular flat-top probe colliding with a flat-top pump as a function of the pump-to-probe waist ratio $w_{0,2}/w_{0,1}$ across the transition. Interpreting the main emission direction (in the branch $\varphi \geq 90°$) as an order parameter, we observe a discontinuous first-order phase transition marked by a finite jump of the order parameter.

parameter while the peak position φ_{peak} serves as an order parameter.

For the case of a Gaussian pump (Fig. 5), the second-order nature of the phase transition is not only confirmed by the qualitative aspects of the graph. We can also quantify the analogy further by fitting the data to a power law as suggested by conventional critical phenomena. Using the fit model

$$\varphi_{\text{peak}}|_{\text{transition}} = C\left(\frac{w_{0,2} - w_{0,2,\text{c}}}{w_{0,1}}\right)^{\beta} + \frac{\pi}{2}, \tag{12}$$

with parameters C, $\boldsymbol{\beta}$, and $w_{0,2,\text{c}}$, we find for the critical exponent of the order parameter $\boldsymbol{\beta} = 0.372 \pm 0.014$. For the critical beam waist, we obtain $w_{0,2,\text{c}}|_{\text{g}} = (4.1736 \pm 0.0037)$ μm, implying a precise result for the critical beam-waist ratio $(w_{0,2,\text{c}}/w_{0,1})|_{\text{g}} = 1.9121 \pm 0.0017$ which plays the role of the critical point. The fit includes all data points of Fig. 5 with $\varphi_{\text{peak}} > 90°$ except for the five right-most points. The errors account for only a part of the discretization errors; see discussion below. In the inset of Fig. 5, the double logarithmic representation demonstrates that the power law Eq. (12) indeed describes the critical region rather accurately over 2 orders of magnitude.

An analytical estimate for the main emission direction for the scenario with a Gaussian pump can be readily extracted from Eq. (3.110) of [63]. Demanding the second derivative of this expression for ϑ to vanish identically, we infer

$$\varphi_{\text{peak}} = \delta\varphi + \frac{\pi}{2}, \tag{13}$$

with $\delta\varphi = 0$ for $w_{0,2} \leq w_{0,2,\text{c}}$ and $\delta\varphi$ implicitly defined by

$$I_1\left(A\frac{w_{0,2}}{\lambda}\delta\varphi\right)\mathrm{e}^{-\frac{1-\nu}{2}\left(\frac{A}{\pi}\right)^2} = \sqrt{\nu} I_1\left(\sqrt{\nu} A \frac{w_{0,2}}{\lambda}\delta\varphi\right) \tag{14}$$

for $w_{0,2} \geq w_{0,2,\text{c}}$. Here, I_1 denotes the modified Bessel function of the first kind and $A = \pi\sqrt{\frac{2(1-1/\mathrm{e})}{1+\nu}}\frac{w_{0,2}}{w_{0,1}}$.

The analytical estimate for the critical beam-waist ratio is [63]

$$(w_{0,2,\text{c}}/w_{0,1})|_{\text{g}} = \sqrt{\frac{1}{1-1/\mathrm{e}}\frac{1+\nu}{1-\nu}\ln(1/\nu)}, \tag{15}$$

which yields $(w_{0,2,\text{c}}/w_{0,1})|_{\text{g}} \simeq 1.9118$ for $\nu = 1/4$ as considered in the present work. Applying the fit model Eq. (12) to the analytical estimate Eq. (13) in the same range (but starting at the critical point) yields $\boldsymbol{\beta} = 0.4370 \pm 0.0038$. For the critical point, we observe a remarkable agreement of the analytical estimate resorting to an *infinite Rayleigh range approximation* with the result of the full numerical calculation. The critical exponent shows a larger deviation. In fact, it is expected that the critical point can be more accurately fitted than the critical exponent since the number and range of data points is small and therefore sufficiently captures only the "location" as a local property but not the "steepness" as an extended feature of the transition. Additionally, it is important to consider that the error in Fig. 5 is significantly smaller than the total numerical error; see discussion below.

We note that the critical point could, of course, be straightforwardly inferred also from the discretized scan of the parameter space. At the current discretization step size, this yields $(w_{0,2,\text{c}}/w_{0,1})|_{\text{g}} = 1.902 \pm 0.014$ which is consistent with the fit result but less precise.

For the case of a flat-top pump, the order parameter undergoes a first-order phase transition analog as shown in Fig. 6. The jump in the order parameter goes hand in hand with the observation of a coexistence region as it is obvious from Fig. 4. The critical point in terms of the critical beam-waist ratio for the flat-top pump setup is given by $(w_{0,2,\text{c}}/w_{0,1})|_{\text{ft}} = 1.930 \pm 0.014$ based on the discretized scan in $w_{0,2}$.

Note that the critical points for the Gaussian pump and the flat-top pump setup are close. Because the flat-top pump considered here can be understood as the limiting case of an infinite-order flattened-Gaussian beam [63,74], the class of flattened-Gaussian beams naturally provides a smooth interpolation between Gaussian and flat-top beams. Therefore, we expect a continuous interpolation between the phase transition analogs in Figs. 5 and 6. Since the flattened-Gaussian beams of order one or higher exhibit an Airy-ring structure, it remains an interesting open question for the future as to whether the transition from second to first order occurs at a critical value of the order of the flattened Gaussian.

As discussed in much more detail in Sec. II B, the computations leading to the results presented in this section are subject to numerical errors and artifacts. With regard to the transverse focus profiles involved, cf. Fig. 2, it is clear that resolving the flat-top beams requires particular care. Since the simulation is confined to a finite volume, we unavoidably lose information. Specifically, cutting off the spatial directions transverse to the beam axes of the driving laser fields goes along with a loss of information that is significant for preserving the relevant beam-profile information.

In the focus, the flat-top structure is encoded in the transversal structure on the fringes of the central peak. Therefore, it is advisable to choose the transversal domain such that the field is cut off at extrema in the focal plane. In this way, the spectral leakage during the FFT_3 caused by the discontinuities in the periodic continuation is minimized. For the estimate of the error $\Delta\varphi_{\mathrm{peak}}$ in Figs. 5 and 6, we have repeated the simulation for a range of values of the transversal length parameters $2w_{0,2,\max} \leq L_{x,z} \lessapprox 18.5 w_{0,2,\max}$. A Richardson extrapolation [75] is then used to obtain an error estimate. Thus, the error corresponds to the limit of accounting for the complete Airy-ring structure of the annular flat-top probe and its effect on the signal's main emission direction, i.e., the qualitative features of the phase transition analogs. A detailed discussion of the variation of $L_{x,z}$ in order to estimate the resulting error is provided in Appendix C.

Additionally, we discuss the impact of the finite propagation lengths $L_{t,y}$ and grid resolution $\Delta\mu$. The estimated errors from these discretization parameters for the qualitative features of Figs. 5 and 6 are found to be small. An estimate for the total discretization error can be obtained by assuming linear convergence in all discretization parameters. In this case, we obtain $(w_{0,2,\mathrm{c}}/w_{0,1})|_{\mathrm{g}} = 1.9065 \pm 0.0066$ and $\boldsymbol{\beta} = 0.417 \pm 0.083$, which is in satisfactory agreement with both the simulation result elaborated above and the analytical estimate. Details are provided in Appendix C.

D. Universality

For the laser pulse collisions studied above, the language of critical phenomena is useful to qualitatively classify the signal emission phenomena as well as to quantify the second-order transition in terms of a critical scaling law and a corresponding critical exponent for the order parameter. This raises the interesting question to which extent the concept of universality applies to the presently studied observables.

For the preceding examples, our results indicate that the qualitative difference between the first- and second-order transitions originates in the transverse focus profile. Increasing the waist of the Gaussian pump, the overlap with the Airy rings of the probe changes smoothly, leading to a smooth transition. By contrast, the overlap for the case of a flat-top pump and the annular probe goes through a sequence of commensurate and incommensurate overlaps, representing a source for a discontinuous transition. Since interpolations between Gaussian and flat-top beam profiles exist in the form of flattened Gaussians [63], it is natural to expect that the observables in the critical region depend on the transversal shape of the pulse. For instance, the critical exponent $\boldsymbol{\beta}$ is likely to depend on the specifics of the beam choice. This would correspond to a lower degree of universality in comparison to critical phenomena in statistical physics.

As an illustration, let us consider again the second-order transition for the case of a Gaussian pump as a function of the blocking fraction ν for the annular flat-top probe beam. It is obvious that the critical exponent $\boldsymbol{\beta}$ cannot be independent of ν: In the limit $\nu \to 0$, the beam turns from annular to standard flat-top form, and thus the phase transition has to vanish. However, for a large blocking fraction $\nu \to 1-\epsilon$, $0 < \epsilon \ll 1$, we expect the phase transition to occur as a stable phenomenon. In order to check for universality, we use the infinite Rayleigh range approximation yielding Eqs. (14) and (15) for an analytical estimate of the critical point and the critical exponent as a function of ν.

Figure 7 displays the value of the critical point in the beam-waist ratio as a function of ν. We observe that the critical point indeed tends to infinity for $\nu \to 0$, implying that the phase transition disappears as expected for $\nu = 0$.

Figure 8 depicts $\boldsymbol{\beta}(\nu)$, exhibiting a large variation for small ν where the phase transition tends to vanish. Interestingly, the critical exponent $\boldsymbol{\beta}(\nu)$ is rather independent of ν for larger values of the blocking fraction where the annular nature of the beam becomes more and more pronounced. In the idealized limit $\nu \to 1^-$ where the

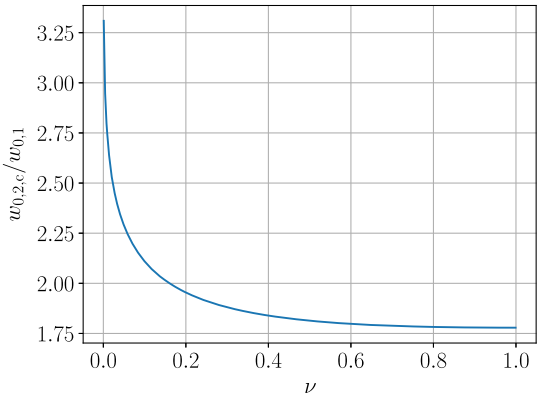

FIG. 7. Analytical estimate Eq. (15) for the location of the critical point in the beam-waist ratio (onset of a second-order phase transition in the emission direction) as a function of the annular-beam blocking fraction ν for the collision with a Gaussian beam. For $\nu \to 0$, the probe beam becomes a flat top, and thus the phase transition disappears. For any value of $\nu \in (0, 1)$, a second-order phase transition is present.

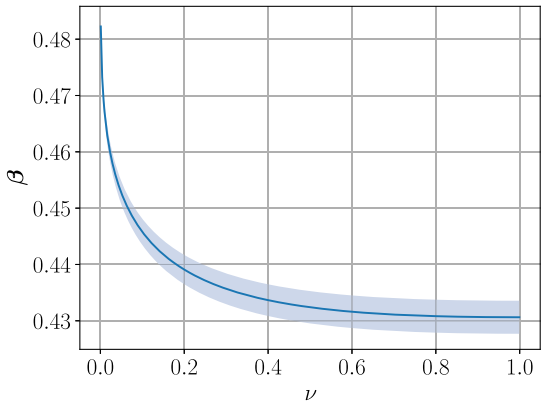

FIG. 8. Analytical estimate based on Eq. (14) for the critical exponent $\boldsymbol{\beta}$ of the second-order phase transition in the emission direction as a function of the annular-beam blocking fraction ν for the collision with a Gaussian beam. An effective universality is observed for larger values of ν, where the far field of the annular probe becomes a thin ring. The blue-shaded region represents the 1σ error band.

annular beam is an infinitesimally thin ring of light in the far field, we approximately find $\boldsymbol{\beta} \simeq 0.43$.

In summary, this simple example demonstrates that the second-order phase transition analog does not extend to quantitative universality in the sense of distinct universality classes characterized by specific values for the critical exponents independent of the precise realization of the phenomenon. Still, we find indications for an effective universality in the sense of the critical exponent depending only weakly on realization details in certain parameter regions.

IV. CONCLUSIONS AND OUTLOOK

We have performed a theoretical study of the quantum vacuum signal attainable in collisions of ultra-intense laser pulses based on the effective action of QED. As an increasing number of petawatt-class lasers are coming online nowadays, increasingly refined theoretical methods in combination with efficient detection schemes are necessary to exploit the full potential of these facilities for the discovery and exploration of the nonlinear response of the quantum vacuum at highest intensities.

In the present work, we demonstrate that the qualitative features of observables can depend strongly on the details of the laser pulses, making the development and use of powerful simulation tools important in the future. For the simple case of a head-on collision of counterpropagating pulses and using a recently proposed dark-field scheme that involves an annular probe, we discovered that observables such as differential numbers of signal photons can undergo the analog of a phase transition as a function of the beam-waist ratio. We highlighted that the nature of this phase transition can depend on the details of the pump beam profile.

The existence of this phase transition analog can be understood from the pulse properties in the focal region that are most relevant for the quantum signal generation. The way that the signal realizes the axisymmetry of the setup depends on how the pump pulse interacts with and thereby resolves the transversal structure of the probe pulse. For a transversally smooth Gaussian pump, we discovered a smooth second-order transition in a signal-photon observable as a function of the pump's beam waist (or equivalently the beam-waist ratio) serving as a control parameter. For a transversally structured flat-top pump, the phase transition is of first order.

In the present example, the language of critical phenomena was also useful to quantify the second-order transition in terms of a critical scaling law and a corresponding critical exponent for the order parameter. In contrast to such critical phenomena in statistical physics, we do not observe an independence of the critical quantities from the details of the pulse collision, and thus, there is no notion of universality classes. Still, we observe an effective universality, i.e., an insensitivity of the critical exponent to specification details in a larger parameter region.

Another difference to conventional phase transitions is reflected in the role and realization of the symmetry: Even though the O(2) axisymmetry is important for the qualitative discussion of the phase transition in the first place, the phase transition does not correspond to an order-disorder transition nor is the symmetry spontaneously broken on one side of the transition. This is because there is no notion of a ground state that may or may not respect the symmetry. Instead, the observables are quantum averages over all possible scattering states, implying that the observables on both sides of the transition fully respect the O(2) symmetry.

As a further important remark, it should be emphasized that the choice of laser parameters made in this work is particularly suitable for the discussion of the phase transition analog. By contrast, the parameters are not optimized for a realistic first-discovery experiment of quantum nonlinearities. For the latter, an optimization of the relative polarization angles, the choice of blocking fraction of the annular beam, and the waist size ratio of the beams would suggest partly very different parameter regimes; see [27,30] for the discussion of concrete detection schemes.

Finally, we stress again that the present work and the quantitative analysis of the partly subtle phenomena have required the use of a reliable numerical simulation code such as the VacEm code together with some performance improvements as well as a careful error analysis as detailed in the appendixes. We believe that the present work serves as a useful example for the use of such codes as well as a motivation for their further development in the future.

ACKNOWLEDGMENTS

We thank Fabian Schütze for valuable discussions. The computational resources were provided by the HPC cluster

Draco of FSU Jena. This work has been funded by the Deutsche Forschungsgemeinschaft (DFG) under Grants No. 392856280, No. 416607684, and No. 416611371 within the Research Unit FOR2783/2.

DATA AVAILABILITY

No data were created or analyzed in this study.

APPENDIX A: UNDERSTANDING AND ADVANCING THE VACEM SIMULATION CODE

The control of the numerical scheme and the subsequent error analysis require a deeper understanding of the VacEm code following [1,44]. There exist two modes of operation: `explicit` and `solver`. As the names suggest, the `explicit` mode computes the signal amplitude based on explicitly defined $\boldsymbol{E}$, $\boldsymbol{B}$ fields. The `solver` mode takes the complex spatial electric-field profile at the focus $\boldsymbol{E}(t_0,\boldsymbol{x})$ as input and propagates it by solving Maxwell's equations in order to provide $\boldsymbol{E}$, $\boldsymbol{B}$ at arbitrary times t. The Maxwell solver was developed in [76]. Note that the theory discussed in Sec. II assumes $\boldsymbol{E}$, $\boldsymbol{B}$ as real fields. Within the VacEm code itself and for the present considerations regarding the Maxwell solver, it is nevertheless convenient to treat the fields as complex; i.e., for the remainder of this section, we assume $\boldsymbol{E}$, $\boldsymbol{B}$ to be complex and use the replacement $\boldsymbol{E} \to \Re(\boldsymbol{E})$, $\boldsymbol{B} \to \Re(\boldsymbol{B})$ in order to make contact with Sec. II.

The propagation is described in terms of the complex spectral amplitudes $a_{0p}(\boldsymbol{k})$ defined by

$$\boldsymbol{A}(t,\boldsymbol{x}) = \int \frac{\mathrm{d}^3\mathrm{k}}{(2\pi)^3} \mathrm{e}^{\mathrm{i}\boldsymbol{k}\cdot\boldsymbol{x}} \hat{\boldsymbol{A}}(t,\boldsymbol{k}), \tag{A1}$$

$$\hat{\boldsymbol{A}}(t,\boldsymbol{k}) = \mathrm{e}^{-\mathrm{i}c\mathrm{k}t} \sum_{p=1}^{2} \boldsymbol{e}_p(\boldsymbol{k}) a_{0p}(\boldsymbol{k}), \tag{A2}$$

where $\boldsymbol{A}(t,\boldsymbol{x})$ is the electromagnetic potential and $\hat{\boldsymbol{A}}(t,\boldsymbol{k})$ its spatial Fourier transform. Any pair of spectral amplitudes corresponds to a solution of Maxwell's equations in vacuum. The code utilizes the radiation gauge, i.e., $A^\mu = (0,\boldsymbol{A})$ and $\nabla\cdot\boldsymbol{A} = 0$. Starting with $\boldsymbol{E}(t_0,\boldsymbol{x})$, the complex spectral amplitudes can be constructed as

$$a_{0p}(\boldsymbol{k}) = \mathrm{e}^{\mathrm{i}c\mathrm{k}t_0} \frac{1}{\mathrm{i}c\mathrm{k}} \boldsymbol{e}_p(\boldsymbol{k}) \cdot \hat{\boldsymbol{E}}(t_0,\boldsymbol{k}). \tag{A3}$$

This representation is not unique; for alternatives, see [1]. The propagated spectral amplitudes are given by

$$a_p(t,\boldsymbol{k}) = \mathrm{e}^{-\mathrm{i}c\mathrm{k}t} a_{0p}(\boldsymbol{k}), \tag{A4}$$

allowing us to compute the propagated $\boldsymbol{E}$, $\boldsymbol{B}$ fields in $\boldsymbol{k}$ space,

$$\hat{\boldsymbol{E}}(t,\boldsymbol{k}) = \mathrm{i}c\mathrm{k}[\boldsymbol{e}_1(\boldsymbol{k}) a_1(t,\boldsymbol{k}) + \boldsymbol{e}_2(\boldsymbol{k}) a_2(t,\boldsymbol{k})], \tag{A5a}$$

$$\hat{\boldsymbol{B}}(t,\boldsymbol{k}) = \mathrm{i}\mathrm{k}[\boldsymbol{e}_1(\boldsymbol{k}) a_2(t,\boldsymbol{k}) - \boldsymbol{e}_2(\boldsymbol{k}) a_1(t,\boldsymbol{k})]. \tag{A5b}$$

An inverse Fourier transform (iFFT_3) of Eq. (A5) then gives us $\boldsymbol{E}$, $\boldsymbol{B}$ at arbitrary times t. Of course, in the `explicit` mode, Eqs. (A1)–(A5) are not required.

These preliminary considerations regarding the Maxwell solver in combination with Sec. II allow us to understand the algorithmic structure of the VacEm code in List. 1.

Listing 1: Pseudocode algorithm of the VacEm code in `solver` mode.

```
INPUT config.ini, E(t_0, x)
a_01, a_02 ⟵ Eq. (A3)(FFT_3(E(t_0, x)))
S_a, S_b ⟵ 0
FOR t = t_start TO t_stop STEP Δt
    a_1, a_2 ⟵ Eq. (A4)(a_01, a_02)
    Ê_i, B̂_i ⟵ Eq. (A5)(a_1, a_2)
    E_i, B_i ⟵ iFFT_3(Ê_i, B̂_i)
    F, G ⟵ Eq. (2)(E_i, B_i)
    Q_i ⟵ Eq. (8a)(E_i, B_i, F, G)
    Q̂_i ⟵ FFT_3(Q_i)
    S_a ⟵ S_a + e^{ickt} e_1 · Q̂
    S_b ⟵ S_b + e^{ickt} e_2 · Q̂
    R_i ⟵ Eq. (8b)(E_i, B_i, F, G)
    R̂_i ⟵ FFT_3(R_i)
    S_a ⟵ S_a − e^{ickt} e_2 · R̂
    S_b ⟵ S_b + e^{ickt} e_1 · R̂
END FOR
S_a ⟵ S_a Δt
S_b ⟵ S_b Δt
OUTPUT S_a, S_b
```

The `explicit` mode features the same algorithm minus the computation of $\boldsymbol{E}$, $\boldsymbol{B}$ and without the need to provide $\boldsymbol{E}(t_0,\boldsymbol{x})$ as input. Reference [1] implemented List. 1 in the programming language `Python 3` [77].

For the present work, two improvements of the VacEm code were implemented; see [44] for details. These are intended to reduce the computational cost. The original VacEm code is already feature-complete within the vacuum emission picture in the sense that it simulates the signal amplitude Eq. (5) for arbitrary EM fields.

The first improvement allows for the use of single-precision floating-point operations (as an alternative to `Python`'s default double precision). Naturally, restricting the float precision to single nearly halves the required memory and reduces the computation time. What makes this a feature for the VacEm code is the fact that the reduction in float precision does not have any adverse effect on the significance of the results. The relative error for double precision is on the order of 10^{-16} (52 bits for the significand, rel. error 2^{-52}) and for single precision 10^{-7}

(23 bits for the significand, rel. error 2^{-23}). Due to accumulation effects, the actual relative error caused by the finite float precision is typically 1 to 2 orders of magnitude larger [FFT_3 error growth is $\mathcal{O}(\log(N_x N_y N_z))$]. For our annular flat-top probe and Gaussian pump setup using single precision, we find no (additional) error for φ_{peak} and a relative error of 10^{-5} for the number of signal photons in the background-free region N_{hole} compared to the double precision result. This precision restriction is well below the analytical error of the one-loop approximation around 10^{-2} and the total numerical error. In fact, when working on predictions for experiments, half-precision floating-point operations could be considered (currently not implemented and therefore not tested). The implementation of single-precision floating-point operations for the VacEm code is only done for the three-dimensional arrays, as all other parts are computationally insignificant in comparison.

The second improvement is multinode parallelism. The original VacEm code employs `pyFFTW` [78] to compute the FFT_3 in parallel. This implementation is restricted to one node. To reduce computation time, we added parallelism to the time integration through `mpi4py` [79]. The allowed values for the number of nodes is restricted to powers of 2. This is due to the parallel data transfer stage. The speedup is close to ideal for a small number of nodes. There are no memory savings. In fact, the full amount of memory required in the original VacEm implementation is now allocated on each node; i.e., the total memory usage scales by the number of nodes plus an additional memory overhead.

As discussed in Sec. II B, the memory per node is the main limiting factor for the VacEm code. A lower bound for the memory usage at double precision is given by [44]

$$\mathrm{RAM}_{\mathrm{min}} = N_x N_y N_z (15 \times 128\ \mathrm{bit} + 8 \times 64\ \mathrm{bit}) \frac{10^{-9}\ \mathrm{GB}}{8\ \mathrm{bit}}, \tag{A6}$$

since 15 `complex128` (a_{01}, a_{02}, $\mathcal{S}_{\mathrm{a}}$, $\mathcal{S}_{\mathrm{b}}$, a_1, a_2, $\boldsymbol{E}$, $\boldsymbol{B}$, $\boldsymbol{Q}$ or $\boldsymbol{R}$) and 8 `double` ($\mathcal{F}$, $\mathcal{G}$, $\boldsymbol{e}_1$, $\boldsymbol{e}_2$) three-dimensional arrays are allocated at the same time. The only scalable way around this problem is FFT_3 with distributed-memory parallelism. For the distributed memory allocation and FFT_3 computation, there already exist multiple libraries. Based on `MPI` and `FFTW`, there are `mpi4py-fft` [80,81], `fftw3-mpi` [65,66], `pfft` [82,83], and `p3dfft++` [84,85], all available through the `Python` wrapper FluidFFT [86,87]. For different FFT_3 implementations including GPU capabilities, see `HeFFTe` [88,89]. Yet, integrating a distributed memory scheme into the current VacEm code structure is not straightforward.

In addition to these generic improvements, there is some potential to optimize the algorithm (List. 1) itself, e.g., making use of in-place operations.

APPENDIX B: STRATEGIES FOR REDUCING NUMERICAL ARTIFACTS

The VacEm code's main operations are the spatial FFT_3 and the temporal rectangle-rule integration used to perform the required space-time integrations. As already previously stated in Sec. II B, the discrete Fourier transform exposes us to aliasing and spectral leakage.

Avoiding aliasing is straightforward by sampling above the Nyquist rate, provided that the maximum frequency in each spatial dimension is known. For the counterpropagating axisymmetric pulse collision setups in this work, we have one propagation direction y and two transversal directions x, z. The maximum wave number in the direction of propagation is $2\pi/\lambda$ plus a bandwidth term $\propto 1/(c\tau)$. In the transversal directions, we only have to resolve wave numbers of the order of $\propto 1/w_0$. Thus, we obtain an estimate of the maximum wave vector $\tilde{k}_{x,y,z}$. For the grid resolution, we find $L_y/N_y \ll L_{x,z}/N_{x,z}$. Our spatial grid sizes at 7.5 points per wavelength range from $63 \times 637 \times 63$ to $360 \times 637 \times 360$ and are therefore comparatively lightweight. The numerical cost of simulations without the symmetry provided by the counterpropagating axisymmetric setup would be much larger since more than one axis needs to resolve $2\pi/\lambda$.

To reduce the effects of spectral leakage, the periodic continuation of the spatial simulation domain should be as smooth as possible. We focus on the annular flat-top probe, as it contributes linearly to the signal amplitude. The cutoff at the boundaries of the simulation domain should be at extremal points of the annular flat-top beam's field amplitude at $t = 0$. Along the propagation direction, we cut off at the next local minimum after $L_y = 6c\tau$. For the transversal directions, we set $L_{x,z} = 2w_{0,2,\mathrm{max}}$ with $w_{0,2,\mathrm{max}} = 8.0\ \mu\mathrm{m}$ as the lower bound and cut off at the next 10 local minima as visualized in Fig. 9. This provides a range of $L_{x,z}$ for the error estimation in Appendix C. In Fig. 9, the black dotted lines show the lower bound, and the gray dotted lines labeled from 0 to 9 show the transverse domain boundaries. As already mentioned, the domain is always determined for $w_{0,2,\mathrm{max}}$ irrespective of the actual pump beam waist. This ensures that the probe is always identically resolved for all pump beam waists, and its resolution is only subject to the changing extents $L_{x,z}$ of the simulation in the transverse directions. On the other hand, for fixed $L_{x,z}$, the pump is best resolved if its beam waist is small. At cutoff 9 used for the results presented in Sec. III C, this effect is of no importance anymore.

At last, we have to consider the number of time steps needed for sufficient convergence of the rectangle-rule integration in time. Of course, resolving the frequency c/λ is required. Significantly more time steps are needed for the rectangle rule to yield a reasonable approximation. We use $N_t = 384$ corresponding to 7.5 points per period, matching the spatial resolution; see [1] for a convergence

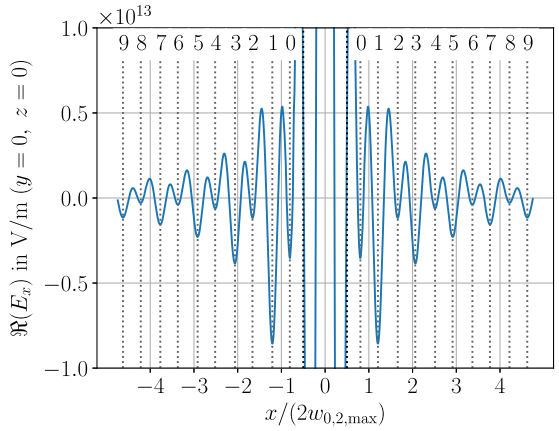

FIG. 9. Spectral leakage is reduced by a suitable adjustment of the boundaries of the simulation domain. In the transversal directions, we choose the axis lengths $L_{x,z}$ such that the boundaries lie in the minima of the probe's focus profile. The gray dotted lines labeled from 0 to 9 depict a sequence of corresponding spatial cutoffs used for our error estimate.

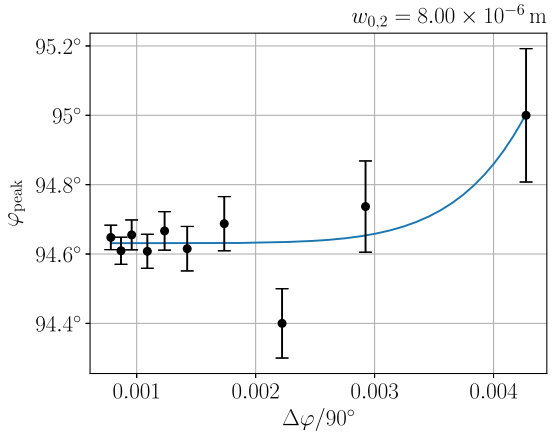

FIG. 10. Convergence of φ_{peak} for the annular flat-top probe and Gaussian pump setup at $w_{0,2} = 8$ μm as a function of the azimuthal resolution $\Delta\varphi$. The blue curve shows the fit of the Richardson extrapolation model Eq. (C1).

analysis of the VacEm code's time integration in the all-optical regime.

Note that in addition to the VacEm code's intrinsic error sources, the evaluation of the simulation data is nontrivial. Most observables relevant to experiment are formulated in spherical coordinates. A mapping from Cartesian to spherical coordinates via interpolation is necessary and can cause artifacts as well as significantly contribute to the total numerical error.

APPENDIX C: ERROR ESTIMATION FOR A MULTIDIMENSIONAL CONVERGENCE PROBLEM

There are eight parameters controlling the simulation grid of the VacEm code. For each of the four axes spanning the simulation grid, there is one length L_μ and one number of points N_μ. Convergence is expected for $L_\mu \to \infty$ and $N_\mu \to \infty$. Focusing on just one parameter, Richardson extrapolation [75] is a universal approach to determine the convergence rate and the extrapolated true value of an observable. Due to the axial symmetry of our setups with regard to the propagation axis (y axis), we can treat the transverse axis lengths $L_{x,z} = 2\pi/k_{x,z} \propto 1/\Delta\varphi$ as one parameter. Strictly speaking, the axial symmetry is broken by the polarization which we choose to lie along the z axis. Yet, an axial symmetry is present for the individual field components, e.g., E_x, E_y, E_z. This is what matters for us since the FFT_3 acts on these field components. For the observable φ_{peak} (now considered as a function of the discretization) in Fig. 5 and 6, the Richardson extrapolation is given by

$$\varphi^*_{\text{peak}} = \varphi_{\text{peak}}\left(\frac{\Delta\varphi}{\pi/2}\right) + C\left(\frac{\Delta\varphi}{\pi/2}\right)^p + O\left(\left(\frac{\Delta\varphi}{\pi/2}\right)^{p+1}\right), \tag{C1}$$

where * marks the extrapolated true value and p is the convergence rate with regard to the discretization (azimuthal resolution or step size) $\Delta\varphi$. At the reference scale $\pi/2$, we get $\frac{\Delta\varphi}{\pi/2} \ll 1$, justifying a truncation at leading order. An example for the convergence fit of the observable φ_{peak} is given in Fig. 10 for the case of the annular flat-top probe and Gaussian pump setup at $w_{0,2} = 8$ μm. Studying the convergence of the VacEm code for different observables, an oscillatory behavior becomes evident. The Richardson model Eq. (C1) is unable to fit these oscillations but still remains a valuable tool for extracting the overall trend, provided that sufficiently many data points are available. In Fig. 10, oscillations dominate at low azimuthal resolution, and therefore the convergence rate cannot be accurately determined; i.e., the relative error in p is greater than 1. Adding more data points is costly and partly constrained by our cutoff requirement discussed in Fig. 9. Nevertheless, we obtain a reasonable estimate of the extrapolated true value; here $\varphi^*_{\text{peak}}|_{\text{Fig.10}} = (94.631 \pm 0.038)°$. In view of these difficulties in model fitting, we use φ^*_{peak} only for error estimation,

$$\Delta\varphi_{\text{peak}} = |\varphi_{\text{peak}} - \varphi^*_{\text{peak}}|. \tag{C2}$$

Equations (C1) and (C2) can be analogously used for other observables and their corresponding discretization. For a less complex and more experimentally relevant observable—the number of signal photons in the background-free region, N_{hole}—we encounter weaker oscillations and therefore

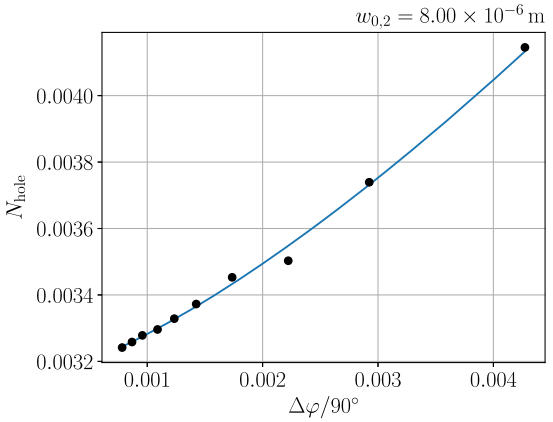

FIG. 11. Convergence of N_{hole} for the annular flat-top probe and Gaussian pump setup at $w_{0,2} = 8$ μm as a function of the azimuthal resolution $\Delta\varphi$. The blue curve shows the fit of the Richardson extrapolation model.

better compatibility with the Richardson model; see Fig. 11. The convergence rate of N_{hole} can be determined as $p|_{\mathrm{Fig.11}} = 1.38 \pm 0.21$. The oscillatory convergence behavior can be understood as an artifact of the discretization—primarily in the context of the FFT_3 but also regarding the construction of a given observable. Increasing $L_{x,z}$ does not just add points to the $\boldsymbol{k}$ space grid but, in general, it readjusts the position of all points, as we keep the grid resolution in coordinate space fixed. Thus, especially angle-dependent observables like φ_{peak} undergo significant oscillations during convergence. Integration along the discretized axes smoothens out this problem; cf. Fig. 11.

A scaling of the remaining simulation parameters gives corrections on the same order of magnitude or smaller for all test cases that we performed. With the annular flat-top probe and Gaussian pump setup, an increase of the grid point density from 7.5 to 9 points per period and wavelength shows relative corrections on the order of 10^{-2} for N_{hole} and 10^{-4} for φ_{peak}. Extending the propagation length $L_{t,y}$ by one pulse duration τ results in 10^{-4} for N_{hole} and no corrections for φ_{peak} (since the mapping to spherical coordinates is identical). In general, each simulation parameter has its own convergence rate for a given observable. A multidimensional convergence analysis according to the Richardson model is given by

$$A^* = A(d_1, \ldots, d_n) + \sum_{i=1}^{n} (C_i d_i^{p_i} + O(d_i^{p_i+1})), \qquad \text{(C3)}$$

with observable A, number of simulation parameters n, discretizations d_i, convergence rates p_i, extrapolated true value A^*, and leading-order constants C_i. Unfortunately, due to the large number $(2n+1)$ of model parameters A^*, p_i, C_i, fitting Eq. (C3) is currently not feasible.

Still, Eq. (C3) can be used to obtain an estimate for the total discretization error in all 8 simulation grid parameters of the VacEm code. The error for a given observable $\Delta A(d_1/s, \ldots, d_n/s)$ at discretizations d_i/s, where $s > 1$ is an arbitrary scaling factor with respect to some base discretization d_i, can be simplified to

$$\Delta A(d_1/s, \ldots, d_n/s) = \left| \frac{A(d_1/s, \ldots, d_n/s) - A(d_1, \ldots, d_n)}{s^p - 1} \right|, \qquad \text{(C4)}$$

under the assumption of an effective convergence rate $p_i = p$. Using $L_t = \tau$, $L_y = 2c\tau$, $L_{x,z} = 10 w_{0,2,\max}$, a temporal resolution of 6 points per period λ/c, and a spatial resolution of 3 points per wavelength $\tilde{k}_{x,y,z}$ as the base discretization before scaling with $s = 2$, we simulate the collision of the annular flat-top probe and Gaussian pump again, now estimating the total discretization error Eq. (C4) for linear convergence $p = 1$. The resulting continuous phase transition in Fig. 12 matches our findings (Fig. 5) from the main text. This estimate is reliable and acts as an upper bound provided that the VacEm code's effective convergence rate $p_{\mathrm{eff}} \geq 1$. This assumption is plausible but needs to be verified case by case.

For N_{hole}, we find a relative error between 7% and 15%. In the case of φ_{peak}, the discretization error in φ due to the mapping from the Cartesian grids at discretizations d_i and $d_i/2$ to spherical coordinates exceeds the estimated total discretization error (which does not take the spherical mapping into account). Therefore, the errors shown in Fig. 12 are the sum of the $\Delta\varphi$ at both discretizations.

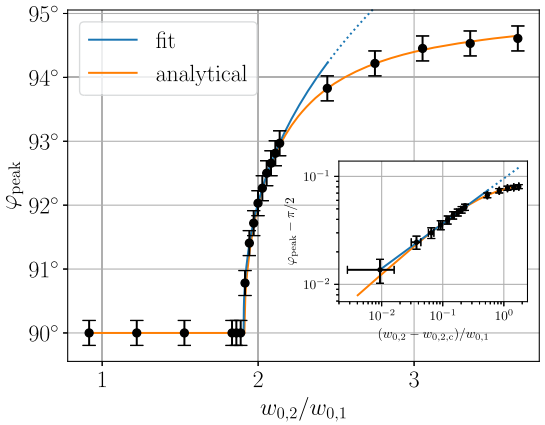

FIG. 12. Main emission direction of the far-field signal-photon distribution for an annular flat-top probe colliding with a Gaussian pump as a function of the pump-to-probe waist ratio $w_{0,2}/w_{0,1}$ across the transition. The figure is completely analogous to Fig. 5 but accounts for errors from all 8 discretization parameters using Eq. (C4) and a linear convergence rate $p = 1$. This yields more conservative estimates for the critical point $(w_{0,2,c}/w_{0,1})|_{\mathrm{g}} = 1.9065 \pm 0.0066$ and the critical exponent $\boldsymbol{\beta} = 0.417 \pm 0.083$, in satisfactory agreement with both the simulation result and the analytical estimate given in the main text.

[1] A. Blinne, H. Gies, F. Karbstein, C. Kohlfürst, and M. Zepf, Phys. Rev. D **99**, 016006 (2019).
[2] W. Heisenberg and H. Euler, Z. Phys. **98**, 714 (1936).
[3] V. Weisskopf, Kong. Dans. Vid. Selsk. Mat. Fys. Medd **14**, 24 (1936).
[4] W. Dittrich and H. Gies, *Probing the Quantum Vacuum: Perturbative Effective Action Approach in Quantum Electrodynamics and Its Application*, Springer Tracts in Modern Physics, Vol. 166 (Springer, Berlin, 2000).
[5] G. V. Dunne, in *From Fields to Strings: Circumnavigating Theoretical Physics: Ian Kogan Memorial Collection (in 3 Volumes)* (World Scientific, Singapore, 2005), pp. 445–522.
[6] A. Di Piazza, K. Z. Hatsagortsyan, and C. H. Keitel, Phys. Rev. Lett. **100**, 010403 (2008).
[7] R. Battesti and C. Rizzo, Rep. Prog. Phys. **76**, 016401 (2013).
[8] B. King and T. Heinzl, High Power Laser Sci. Eng. **4**, e5 (2016).
[9] F. Karbstein, Particles **3**, 39 (2020).
[10] A. Fedotov, A. Ilderton, F. Karbstein, B. King, D. Seipt, H. Taya, and G. Torgrimsson, Phys. Rep. **1010**, 1 (2023).
[11] H. Euler and B. Kockel, Naturwissenschaften **23**, 246 (1935).
[12] R. Karplus and M. Neuman, Phys. Rev. **80**, 380 (1950).
[13] R. Karplus and M. Neuman, Phys. Rev. **83**, 776 (1951).
[14] B. De Tollis, Nuovo Cimento **35**, 1182 (1965).
[15] E. Lundström, G. Brodin, J. Lundin, M. Marklund, R. Bingham, J. Collier, J. T. Mendonça, and P. Norreys, Phys. Rev. Lett. **96**, 083602 (2006).
[16] B. King, A. Di Piazza, and C. H. Keitel, Nat. Photonics **4**, 92 (2010).
[17] B. King and C. H. Keitel, New J. Phys. **14**, 103002 (2012).
[18] F. Karbstein, H. Gies, M. Reuter, and M. Zepf, Phys. Rev. D **92**, 071301 (2015).
[19] S. Ataman, Phys. Rev. A **97**, 063811 (2018).
[20] R. Aboushelbaya *et al.*, Phys. Rev. Lett. **123**, 113604 (2019).
[21] F. Karbstein and E. A. Mosman, Phys. Rev. D **101**, 113002 (2020).
[22] C. K. Dumlu, Y. Nakamiya, and K. A. Tanaka, Phys. Rev. D **106**, 116001 (2022).
[23] F. Karbstein, D. Ullmann, E. A. Mosman, and M. Zepf, Phys. Rev. Lett. **129**, 061802 (2022).
[24] C. Sundqvist and F. Karbstein, Phys. Rev. D **108**, 056028 (2023).
[25] M. Formanek, J. P. Palastro, D. Ramsey, S. Weber, and A. Di Piazza, Phys. Rev. D **109**, 056009 (2024).
[26] A. J. Macleod and B. King, Phys. Rev. A **110**, 032216 (2024).
[27] F. Schütze, L. Doyle, J. Schreiber, M. Zepf, and F. Karbstein, Phys. Rev. D **109**, 096009 (2024).
[28] J. Peatross, J. L. Chaloupka, and D. D. Meyerhofer, Opt. Lett. **19**, 942 (1994).
[29] M. Zepf, G. D. Tsakiris, G. Pretzler, I. Watts, D. M. Chambers, P. A. Norreys, U. Andiel, A. E. Dangor, K. Eidmann, C. Gahn, A. Machacek, J. S. Wark, and K. Witte, Phys. Rev. E **58**, R5253 (1998).
[30] N. Ahmadiniaz *et al.*, arXiv:2405.18063.
[31] A. Gonoskov, T. G. Blackburn, M. Marklund, and S. S. Bulanov, Rev. Mod. Phys. **94**, 045001 (2022).
[32] H. Gies, F. Karbstein, and C. Kohlfürst, Phys. Rev. D **97**, 036022 (2018).
[33] B. King, H. Hu, and B. Shen, Phys. Rev. A **98**, 023817 (2018).
[34] F. Karbstein, C. Sundqvist, K. S. Schulze, I. Uschmann, H. Gies, and G. G. Paulus, New J. Phys. **23**, 095001 (2021).
[35] T. Grismayer, R. Torres, P. Carneiro, F. Cruz, R. Fonseca, and L. O. Silva, New J. Phys. **23**, 095005 (2021).
[36] A. Lindner, B. Ölmez, and H. Ruhl, Software Impacts **15**, 100481 (2023).
[37] A. M. Lindner, Simulating the nonlinear QED vacuum, Ph.D. thesis, Munich U., 2023.
[38] D. Galtsov and V. Skobelev, Phys. Lett. **36B**, 238 (1971).
[39] F. Karbstein and R. Shaisultanov, Phys. Rev. D **91**, 113002 (2015).
[40] A. Sainte-Marie, L. Fedeli, N. Zaïm, F. Karbstein, and H. Vincenti, New J. Phys. **24**, 065005 (2022).
[41] A. V. Berezin and A. M. Fedotov, Phys. Rev. D **110**, 016009 (2024).
[42] F. Karbstein, A. Blinne, H. Gies, and M. Zepf, Phys. Rev. Lett. **123**, 091802 (2019).
[43] M. Valialshchikov, F. Karbstein, D. Seipt, and M. Zepf, Phys. Rev. D **110**, 076009 (2024).
[44] L. Maiwald, All-optical signatures of quantum vacuum nonlinearities in numerical simulations of unexplored regimes, M.Sc. thesis, Friedrich-Schiller-Universität Jena, Jena, 2023.
[45] L. P. Kadanoff, in *From Order To Chaos: Essays: Critical, Chaotic and Otherwise* (World Scientific, Singapore, 1993), pp. 222–239.
[46] K. G. Wilson and J. B. Kogut, Phys. Rep. **12**, 75 (1974).
[47] J. Zinn-Justin, Int. Ser. Monogr. Phys. **113**, 1 (2002).
[48] M. W. Choptuik, Phys. Rev. Lett. **70**, 9 (1993).
[49] C. Gundlach and J. M. Martin-Garcia, Living Rev. Relativity **10**, 5 (2007).
[50] H. Gies and G. Torgrimsson, Phys. Rev. Lett. **116**, 090406 (2016).
[51] H. Gies and G. Torgrimsson, Phys. Rev. D **95**, 016001 (2017).
[52] A. Ilderton, G. Torgrimsson, and J. Wárdh, Phys. Rev. D **92**, 065001 (2015).
[53] S. P. Gavrilov, D. M. Gitman, and A. A. Shishmarev, Phys. Rev. D **99**, 116014 (2019).
[54] T. C. Adorno, Z.-W. He, S. P. Gavrilov, and D. M. Gitman, J. High Energy Phys. 12 (**2021**) 046.
[55] T. W. Baumgarte, B. Brügmann, D. Cors, C. Gundlach, D. Hilditch, A. Khirnov, T. Ledvinka, S. Renkhoff, and I. S. Fernández, Phys. Rev. Lett. **131**, 181401 (2023).
[56] D. Cors, S. Renkhoff, H. R. Rüter, D. Hilditch, and B. Brügmann, Phys. Rev. D **108**, 124021 (2023).
[57] K. Marouda, D. Cors, H. R. Rüter, F. Atteneder, and D. Hilditch, Phys. Rev. D **109**, 124042 (2024).
[58] G. Degli Esposti and G. Torgrimsson, Phys. Rev. D **110**, 076017 (2024).
[59] J. Schwinger, Phys. Rev. **82**, 664 (1951).
[60] V. I. Ritus, Sov. Phys. JETP **42**, 774 (1975).
[61] W. Dittrich and M. Reuter, *Effective Lagrangians in Quantum Electrodynamics* (Springer, New York, 1985), Vol. 220.

[62] H. Gies and F. Karbstein, J. High Energy Phys. 03 (2017) 108.
[63] F. Karbstein, Quantum vacuum nonlinearities in strong electromagnetic fields, Habilitation thesis, Friedrich-Schiller-Universität Jena, 2023.
[64] D. Efnusheva, A. Cholakoska, and A. Tentov, Int. J. Comput. Sci. Inf. Technol. **9**, 151 (2017).
[65] FFTW, https://www.fftw.org/.
[66] M. Frigo and S. Johnson, Proc. IEEE **93**, 216 (2005).
[67] F. Karbstein and E. A. Mosman, Phys. Rev. D **100**, 033002 (2019).
[68] A. Di Piazza, K. Z. Hatsagortsyan, and C. H. Keitel, Phys. Rev. D **72**, 085005 (2005).
[69] A. M. Fedotov and N. B. Narozhny, Phys. Lett. A **362**, 1 (2007).
[70] H. Gies, F. Karbstein, and R. Shaisultanov, Phys. Rev. D **90**, 033007 (2014).
[71] P. Böhl, B. King, and H. Ruhl, Phys. Rev. A **92**, 032115 (2015).
[72] H. Gies, F. Karbstein, and N. Seegert, Phys. Rev. D **93**, 085034 (2016).
[73] P. V. Sasorov, F. Pegoraro, T. Z. h. Esirkepov, and S. V. Bulanov, New J. Phys. **23**, 105003 (2021).
[74] F. Gori, Opt. Commun. **107**, 335 (1994).
[75] L. F. Richardson, Phil. Trans. R. Soc. A **210**, 307 (1911).
[76] A. Blinne, S. Kuschel, S. Tietze, and M. Zepf, J. Comput. Phys. X **1**, 100019 (2019).
[77] Python, https://www.python.org/.
[78] pyFFTW, https://github.com/pyFFTW/pyFFTW.
[79] Mpi4py, https://github.com/mpi4py/mpi4py.
[80] Mpi4py-fft, https://github.com/mpi4py/mpi4py-fft.
[81] L. Dalcin, M. Mortensen, and D. E. Keyes, Fast parallel multidimensional FFT using advanced MPI (2018).
[82] PFFT, https://github.com/mpip/pfft.
[83] M. Pippig, SIAM J. Sci. Comput. **35**, C213 (2013).
[84] P3DFFT++, https://github.com/sdsc/p3dfft.3.
[85] D. Pekurovsky, SIAM J. Sci. Comput. **34**, C192 (2012).
[86] FluidFFT, https://github.com/fluiddyn/fluidfft.
[87] A. V. Mohanan, C. Bonamy, and P. Augier, J. Open Res. Software **7**, 10 (2019).
[88] HeFFTe, https://github.com/af-ayala/heffte.
[89] A. Ayala, S. Tomov, A. Haidar, and J. Dongarra, in *Computational Science—ICCS 2020*, edited by V. V. Krzhizhanovskaya, G. Závodszky, M. H. Lees, J. J. Dongarra, P. M. A. Sloot, S. Brissos, and J. Teixeira (Springer International Publishing, Cham, 2020), pp. 262–275.